

Article

Constructing Co Cluster Sites for Selective CO₂ Hydrogenation via Phase Segregation from Co-Doped TiO₂ Nanocrystals

Xiangru Wei¹, Yizhen Chen¹, Yulu Zhang¹, Liyue Zhang¹, Lu Ma², Matthew M. Yung³, and Sen Zhang^{1,*}

¹ Department of Chemistry, University of Virginia, Charlottesville, VA 22904, USA

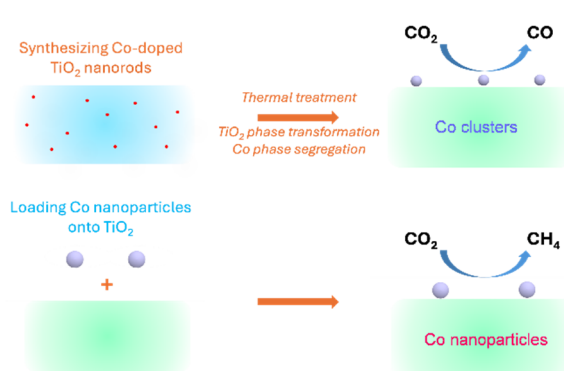
² National Synchrotron Light Source II, Brookhaven National Laboratory, Upton, NY 11973, USA

³ Bioenergy Science and Technology Directorate, National Renewable Energy Laboratory, Denver West Parkway, Golden, CO 80401, USA

* Correspondence: sz3t@virginia.edu

Received: 7 November 2024; Revised: 2 January 2025; Accepted: 3 January 2025; Published: 23 January 2025

Abstract: This article presents a Co phase segregation strategy for creating stable Co cluster catalytic sites on TiO₂, enabling selective CO₂ hydrogenation to CO. Through oxidative calcination, pre-synthesized Co-doped brookite TiO₂ nanorods transform into a mixed TiO₂ phase, leading to the phase segregation of Co species. The resulting Co clusters, stabilized by strong Co-TiO₂ interactions during reductive CO₂ hydrogenation, effectively suppress the formation of larger nanoparticles. The undercoordinated sites of these clusters promote a high CO production rate with near-unit selectivity, contrasting with Co nanoparticles, which favor CH₄ formation under identical conditions. In-situ diffuse reflectance infrared Fourier transform spectroscopy (DRIFTS) analysis indicates that the weakened CO adsorption on Co clusters is key to their enhanced CO selectivity, highlighting this method as a promising approach for efficient CO₂ utilization.



Keywords: CO₂ hydrogenation; heterogeneous catalysis; cluster sites; selectivity; phase segregation.

1. Introduction

CO₂ valorization technologies are becoming increasingly critical for mitigating the environmental impact of carbon emission and promoting a circular carbon economy [1,2]. At the heart of this approach is the utilization of CO₂ as a feedstock, along with renewable hydrogen and energy sources, to produce valuable carbon-based chemicals and fuels, reducing reliance on fossil-derived resources [3–5]. Typically, CO₂ hydrogenation at atmospheric pressure proceeds through the reverse water-gas shift (RWGS) reaction ($\text{CO}_2 + \text{H}_2 \rightarrow \text{CO} + \text{H}_2\text{O}$) and the methanation reaction ($\text{CO}_2 + 4\text{H}_2 \rightarrow \text{CH}_4 + 2\text{H}_2\text{O}$), yielding CO and CH₄, respectively [6]. There has been significant interest in enhancing selectivity for CO production over CH₄, as CO is a crucial intermediate in the synthesis of liquid hydrocarbons and oxygenated products [6–8].

Research indicates that various metals, including Rh [9–11], Ru [12,13], Ni [14,15] and Pd [16] tend to favor CO production over CH₄ when present as smaller nanoparticles rather than larger ones. For example, Simons et al. [17] investigated Ni catalysts of varying nanoparticle sizes (2–12 nm) supported on silica using operando spectroscopy to explore their structure-sensitivity of CO₂ hydrogenation. They found that the active sites involved in the conversion of CO₂ to CO differ from those responsible for the subsequent hydrogenation of CO to CH₄. While the initial CO₂-to-CO reaction is minimally influenced by nanoparticle size, the hydrogenation of CO to CH₄ is highly sensitive to the structure. Specifically, nanoparticles smaller than 5 nm have a reduced availability of step edges, which are essential for CO dissociation, leading to a significant decrease in methanation activity. Such findings are widely accepted in mechanistic studies of the methanation reaction [18–20], suggesting that CO₂ often first dissociates to CO via the RWGS reaction, with the adsorbed CO serving as a key intermediate in CH₄ formation



Copyright: © 2025 by the authors. This is an open access article under the terms and conditions of the Creative Commons Attribution (CC BY) license (<https://creativecommons.org/licenses/by/4.0/>).

Publisher's Note: Scilight stays neutral with regard to jurisdictional claims in published maps and institutional affiliations.

through direct C–O bond cleavage or the RWGS + CO-Hydro pathway [21,22]. In the direct C–O bond cleavage pathway, *CO_2 dissociates to *CO and *O , and the resulting *CO undergoes further dissociation to form *O and *C , which is subsequently hydrogenated to CH_4 [23,24]. Alternatively, *CO can be hydrogenated to *HCO , which dissociates into $^*CH + ^*O$, with *CH eventually being hydrogenated to CH_4 [25,26].

The Co-based catalyst has been widely used for multiple CO_2 hydrogenation reactions, such as methanation [27], methanol synthesis [28], and C–C coupling reactions including Fischer–Tropsch synthesis [29] and higher alcohol synthesis [30]. However, a comprehensive understanding of the structure–property relationships in Co-based catalytic systems for RWGS reaction remains limited, posing challenges for the rational design, optimization, and mechanistic elucidation of these catalysts. Compared to metallic nanoparticles, we envision that smaller clusters, characterized by primarily low coordination sites, hold promise for reducing the likelihood of multi-bound CO adsorption—a crucial step in CH_4 production [31]. To produce these small Co cluster catalysts, we developed a Co phase segregation strategy aimed at limiting nanoparticle formation and enhancing cluster stability. To achieve this, we synthesized Co-doped TiO_2 (Co- TiO_2) nanorods using a one-step colloidal method, where Co atoms are integrated into TiO_2 brookite nanorods through single-site substitution, forming stable Co–O–Ti bonds. X-ray absorption spectroscopy (XAS) and synchrotron X-ray diffraction (SXRD) analyses showed that oxidative calcination induces the phase transformation of brookite TiO_2 while simultaneously promoting Co phase segregation, as illustrated in Figure 1. The robust Co/ TiO_2 interactions help stabilize Co clusters, preventing the formation of larger nanoparticles under reductive CO_2 hydrogenation conditions, which results in improved CO selectivity. In-situ diffuse reflectance infrared Fourier transform spectroscopy (DRIFTS) further revealed that the weakened CO adsorption on Co clusters, compared to larger nanoparticles, is a critical factor contributing to the enhanced CO selectivity during CO_2 hydrogenation.

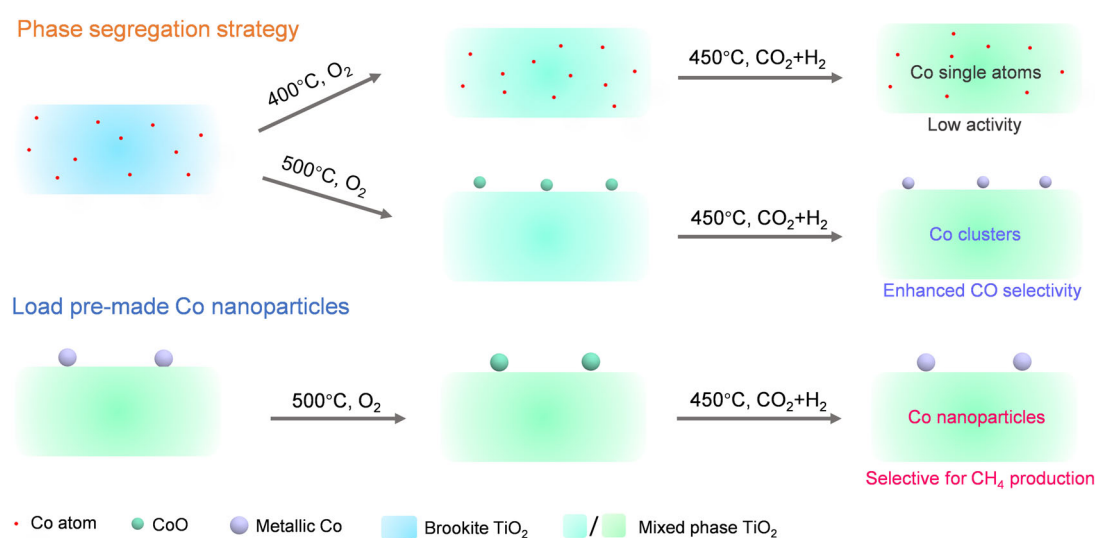


Figure 1. Schematic illustration of the development of Co cluster catalysts for CO production through the segregation of Co from Co- TiO_2 . In contrast, depositing Co nanoparticles onto a TiO_2 support results in CH_4 production.

2. Results and Discussion

The Co- TiO_2 nanorods were synthesized through thermal decomposition of titanium chloride ($TiCl_4$) and cobalt oleate precursors in an octadecane (ODE) solution, with oleylamine (OAm) and oleic acid (OAc) as surfactants, following a previously established protocol [32,33]. During high-temperature synthesis, a minor release of water, resulting from the reaction between OAc and OAm, facilitates the controlled hydrolysis of $TiCl_4$. Simultaneously, cobalt oleates decompose, leading to the formation of TiO_2 nanorods doped with Co atoms.

By adjusting the ratio of Co to Ti precursors, Co- TiO_2 nanorods with varying doping concentrations were achieved, reaching a maximum Co doping level of approximately 12%, as reported in our earlier studies [33]. Transmission electron microscopy (TEM, Thermo Fisher Scientific, Waltham, MA, USA) images confirm that Co- TiO_2 nanorods with different Co doping levels retain a consistent nanorod morphology, exhibiting an average diameter of 4.2 ± 0.8 nm and an average length of 35 ± 6 nm (Figures 2a and S1). Synchrotron X-ray diffraction (SXRD, Brookhaven National Laboratory, Upton, NY, USA) analysis ($\lambda = 0.6199$ Å) (Figure 2b) reveals the exclusive formation of the brookite phase of TiO_2 , as indicated by the characteristic (121) diffraction peak at 12.28° (2θ) (JCPDS file: 96-900-4143), with no interference from anatase or rutile phases. For comparison, Co

nanoparticles (NPs) with an average size of 8.2 ± 2 nm were synthesized (Figure S2a) and subsequently loaded onto a commercial TiO₂ support (P25), yielding the reference sample, Co NPs/TiO₂ (Figure S2b) [34].

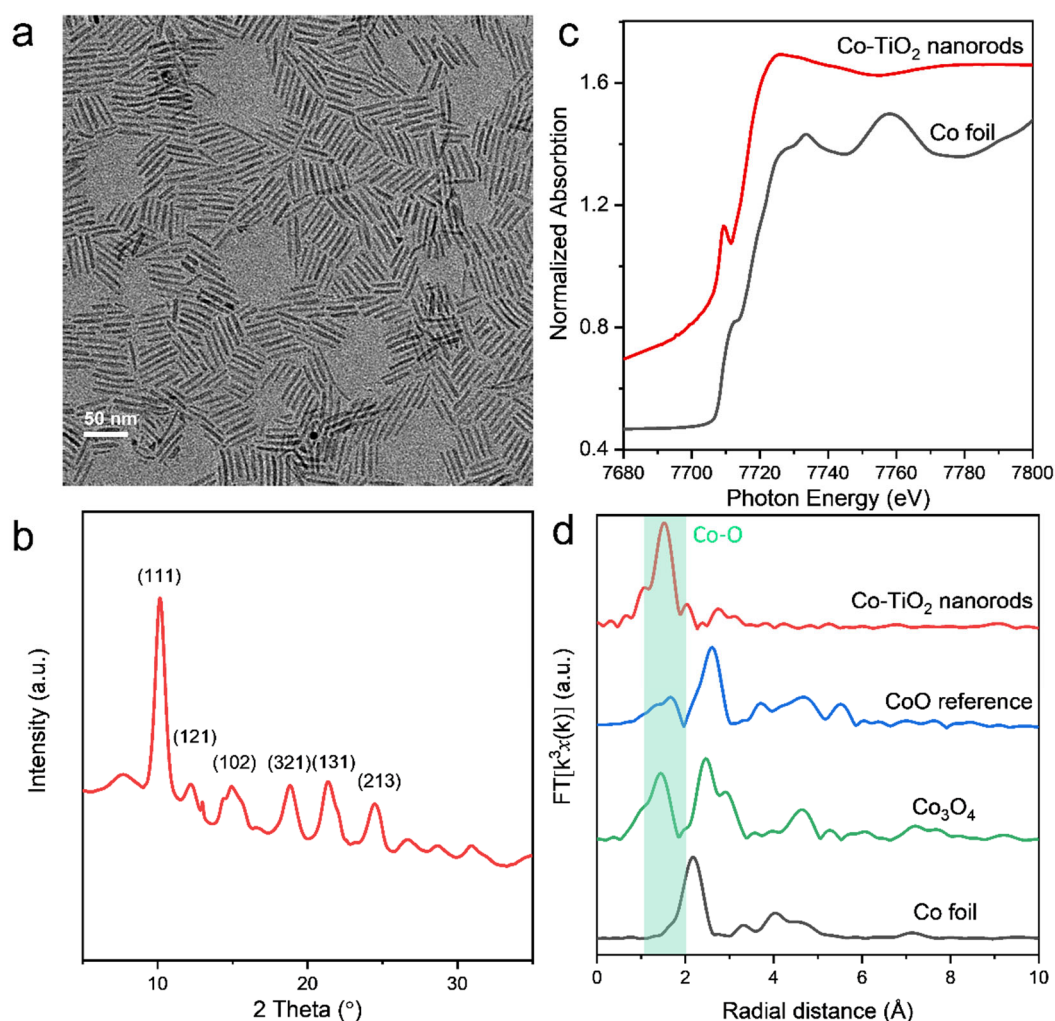


Figure 2. Characterization of as-synthesized Co-TiO₂ (12%) nanorods. (a) TEM image, (b) synchrotron X-ray diffraction (SXR D) pattern, (c) Co K-edge X-ray absorption near-edge structure (XANES) profiles, and (d) k^3 -weighted Fourier transform of extended X-ray absorption fine structure (EXAFS) spectra of Co-TiO₂ nanorods and reference samples.

The electronic structures, oxidation states, and local bonding environments of the Co species in Co-TiO₂ nanorods were further investigated using Co K-edge X-ray absorption near-edge structure (XANES) and extended X-ray absorption fine structure (EXAFS) spectroscopies. The XANES spectra (Figure 2c) are consistent with previously reported findings, indicating that the oxidation state of Co in the as-synthesized Co-TiO₂ nanorods is predominantly Co²⁺, distinct from the Co⁰ state observed in Co foil [35]. Additionally, the corresponding EXAFS spectra (Figure 2d) of the as-synthesized Co-TiO₂ nanorods exhibit similar characteristics to prior studies [33], confirming that the Co species are primarily isolated Co atoms doped within the TiO₂ matrix, with no detectable contributions from metallic Co or Co oxides.

Prior to catalytic testing, the Co-TiO₂ nanorods were subjected to calcination at various temperatures (400–600 °C) in air for 2 h to remove surfactants from the colloidal nanocrystals and expose the active catalyst surface, yielding Co-TiO_{2-x} (where x denotes the oxidative calcination temperature). The calcined samples were then reduced in situ under reaction conditions (1 vol.% CO₂ + 4 vol.% H₂ + 95 vol.% N₂) at 450 °C before the study of CO₂ hydrogenation. It was observed that the nanorod morphology was largely preserved after calcination at 400 °C (Figure S3a). However, increasing the temperature to 500 °C resulted in pronounced aggregation, forming irregular nanosheets, with further coalescence observed following calcination at 600 °C (Figure S3b,c).

SXR D analysis suggests that these morphological changes are coupled with phase transitions in TiO₂. As shown in Figure S4, using the representative sample Co-TiO₂₋₅₀₀, the crystallinity of the catalyst is enhanced after calcination, and the brookite phase partially transforms into rutile and anatase. This transformation is evidenced

by the presence of the (110) diffraction peak of rutile at 10.93° (JCPDS file: 96-900-4143) and the (200) diffraction peak of anatase at 18.86° (JCPDS file: 96-900-8214). After reduction under the reaction gas, the intensity of the brookite peaks at 12.28° further diminished, indicating a continued phase transformation from brookite to rutile and anatase. Notably, no diffraction peaks corresponding to cobalt species such as CoO, Co_3O_4 , or metallic Co were detected, even in the sample with a high Co doping level (12%) calcined at 500°C (Figure S4). This indicates that, despite potential Co segregation from the TiO_2 matrix during the calcination process, the Co species do not form large grains with long-range crystalline order. We observed that higher calcination temperatures facilitated phase transitions, with a larger fraction of brookite converting into anatase and rutile when calcined at 600°C . This process led to a more pronounced mixed-phase composition, as shown in Figure S5.

The CO_2 hydrogenation performance of each catalyst was evaluated over a temperature range of 250 to 500°C in a fixed-bed reactor. Pure TiO_2 showed no measurable CO_2 conversion under these conditions. As shown in Figure 3a,b, the Co NPs/ TiO_2 catalyst predominantly promotes CO_2 methanation, achieving a high CH_4 selectivity of 81.2% at 400°C . In contrast, the Co- TiO_2 -500 catalyst (12% Co) exhibits near-complete selectivity for CO across the entire temperature range. Specifically, at 450°C and a CO_2 conversion of 40.9%, the CO selectivity reaches 98.7%. This shift in product distribution suggests that the Co- TiO_2 significantly suppresses the deep hydrogenation of CO to CH_4 , favoring the production of CO as the primary hydrogenation product [36,37]. As shown in Figure 3c, the Co- TiO_2 -500 catalyst maintains its high CO selectivity throughout a 10-h continuous reaction while preserving its morphology (Figure S6). This demonstrates the catalyst's robust stability under CO_2 hydrogenation conditions.

To investigate the effect of Co loading on catalytic performance, Co- TiO_2 -500 catalysts with varying Co concentrations but constant Co mass (143 mg of 4.2% Co- TiO_2 , 80 mg of 7.5% Co- TiO_2 , and 50 mg of 12% Co- TiO_2) were tested. As shown in Figure S7, the catalytic activity and CO selectivity remained largely unaffected by changes in Co loading. However, calcination temperature was found to significantly influence performance, as illustrated in Figure S8. The Co- TiO_2 -400 sample exhibits low activity, achieving a CO_2 conversion of only 8.9% at 400°C . With increasing calcination temperature, CO_2 conversion rates improve, reaching 28.6% and 40.1% for the Co- TiO_2 -500 and Co- TiO_2 -600 samples, respectively. Simultaneously, the Co- TiO_2 -600 catalyst shows a higher CH_4 selectivity (9.9% at 400°C) compared to other calcined samples.

To elucidate the origins of the distinct catalytic activity and selectivity, EXAFS experiments were performed to monitor structural changes in Co- TiO_2 catalysts exposed to varying calcination temperatures. In the case of the Co- TiO_2 -400 sample, the EXAFS spectrum shows a predominant, single Co–O shell, which is consistent with the as-synthesized nanorods, indicating that the atomically dispersed Co structure remains stable at 400°C (Figure 4a). However, after the calcination at 500°C in air, phase segregation of the Co species was observed. The Co K-edge EXAFS spectrum of Co- TiO_2 -500 showed not only the Co–O pathway but also the presence of multiple shells at higher distance, R (Figure 4a). These shells correspond to Co–O–Co scattering pathways similar to those found in reference materials like Co_3O_4 and CoO [38,39]. Notably, the distinct second and third shells were observed that shifted to a higher R position than the Co–O–Co, suggesting the formation of Co–O–Ti structures due to high-temperature calcination, which implies strong bonding interactions between Co and the TiO_2 support [40,41]. These results suggest that Co species in the Co- TiO_2 -500 primarily exist as CoO_x clusters on TiO_2 . Moreover, the absence of observable cobalt oxide XRD peaks, as previously mentioned, further supports the presence of small CoO_x clusters after oxidative calcination [42].

As shown in Figure 4b, the XANES spectrum of the reduced Co- TiO_2 -500 sample (under CO_2 hydrogenation conditions) exhibits a decrease in white-line intensity and pre-edge features, indicating the reduction of Co species following the reaction process. The corresponding EXAFS analysis reveals the appearance of a small shell (Figure 4a), consistent with the Co–Co shell in Co foil, further confirming the reduction of CoO_x clusters. Although our ex-situ XAS experiments involved air exposure, which may have caused some oxidation during sample transfer, this subtle change observed in the XAS result suggests that reduced Co metallic clusters are likely the active species under CO_2 hydrogenation conditions. However, due to the small size of the Co clusters, no metallic Co peaks are detected in the XRD pattern of the reduced Co- TiO_2 -500 sample (Figure S4). In contrast, the Co NPs/ TiO_2 sample clearly exhibits Co peaks in its XRD pattern (Figure S9), indicating larger Co nanoparticles.

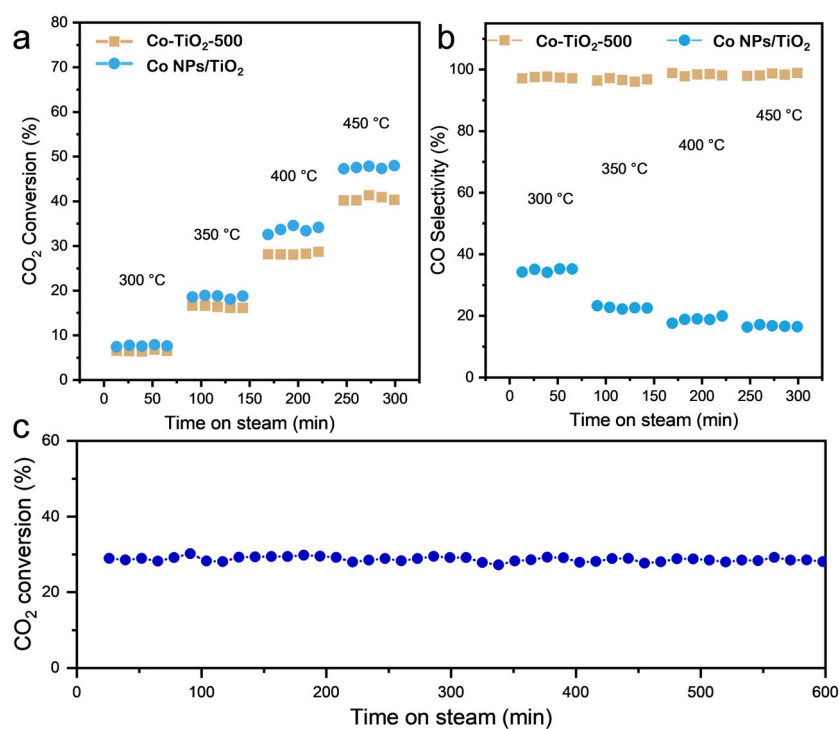


Figure 3. Catalytic performance of Co-TiO₂-500 (12%) and Co NPs/TiO₂ catalysts. (a) CO₂ conversion and (b) CO selectivity with time on stream at different temperatures. (c) Stability test for CO₂ hydrogenation over Co-TiO₂-500 (12%) catalyst. Reaction conditions: 1 vol % CO₂ + 4 vol % H₂ + 95 vol % N₂ with a space velocity of ~30,000 mL g_{cat}⁻¹ h⁻¹ at ambient pressure, 400 °C.

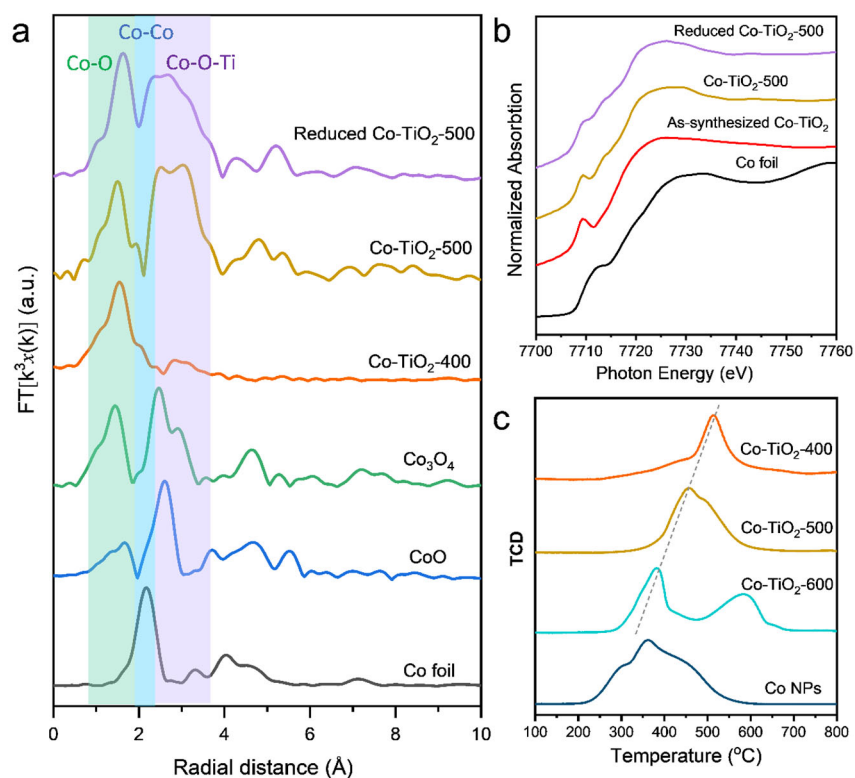


Figure 4. (a) k^3 -weighted Fourier transform of EXAFS and (b) XANES spectra of the catalysts and reference samples. (c) H₂-TPR profiles of the catalysts.

The phase segregation of Co from the Co-TiO₂ support is a critical process in forming the desirable cluster structure. Unlike catalysts prepared through post-loading methods, the strong interaction between the TiO₂ support and Co species effectively limits the size of segregated Co, stabilizing them in a cluster state under CO₂

hydrogenation conditions and preventing their growth into larger particles. As a result, the Co-TiO₂-500 catalyst achieves near-unit selectivity for CO production. Even with further intensified Co segregation and potential aggregation into nanoparticles at 600 °C, the Co-TiO₂-600 catalyst continues to exhibit much higher selectivity for CO over CH₄ than Co NPs/TiO₂.

H₂ temperature-programmed reduction (H₂-TPR) was performed to investigate the interaction strength between Co and the TiO₂ support (Figure 4c). The Co NPs/TiO₂ catalyst exhibits a broad reduction peak between 200 and 500 °C. The peak at 200–350 °C can be attributed to the reduction of Co³⁺ to Co²⁺, while the peak at 350–500 °C corresponds to the reduction of Co²⁺ to Co⁰ (both in the surface and inner layers) [43]. In comparison, the Co reduction temperatures for the Co-TiO₂-400 catalyst are significantly higher, indicating the limited reducibility of single-site Co dopant in TiO₂ matrix [44]. The Co phase segregation from TiO₂ matrix, as demonstrated by the shift of the reduction peak to lower temperatures in Co-TiO₂-500 and Co-TiO₂-600 catalyst. In the Co-TiO₂-600 catalyst, a reduction peak around 390 °C, associated with CoO_x reduction, is observed, along with an additional peak at 590 °C, which may be attributed to the formation of CoTiO₃ at high temperature [45].

In-situ diffuse reflectance infrared Fourier transform spectroscopy (DRIFTS) studies were conducted under steady-state CO₂ hydrogenation conditions on both Co-TiO₂-500 and Co NPs/TiO₂ catalysts to further understand the origins of their differing selectivities. As shown in Figure 5, upon introducing the reaction gas mixture (1 vol.% CO₂, 4 vol.% H₂, and 95 vol.% N₂) at 300 °C, symmetric OCO stretching of bicarbonate (HCO₃⁻) and carbonate (CO₃²⁻) species (1565 cm⁻¹, 1362 cm⁻¹) are immediately observed on the surfaces of both catalysts, indicating the interaction between CO₂ and hydroxyl groups on TiO₂ [46]. On the Co NPs/TiO₂ catalyst, a band at 1965 cm⁻¹ appears, corresponding to multi-bound CO on hollow Co sites (Figure 5a, at 1 min). Simultaneously, methane formation is detected, evidenced by the emergence of C–H bonds (3013 cm⁻¹) [26]. As the reaction progressed, the intensities of the CO and C–H bands increase (Figure 5a, at 5–60 min), signifying an accelerating CO₂ methanation reaction. Additionally, weak and unchanged bands associated with formate (HCOO⁻) species at 2962 and 2878 cm⁻¹ are observed, suggesting that formate is not a reaction intermediate [47]. In contrast, when the same experiment was performed on Co-TiO₂ (Figure 5b), CO is detected as the primary product after the introduction of the reactant gas. However, no CO band appears in the DRIFTS spectrum, indicating that CO immediately desorbs from the catalyst as the final product. The absence of C–H bands further confirms that the hydrogenation of CO to methane is strongly suppressed in the Co-TiO₂ system (Figure 5b).

The in-situ DRIFTS results suggest that differences in CO interaction strength may account for the selectivity variations between the two catalysts. On Co-TiO₂, rapid CO desorption prevents further hydrogenation to methane, making CO the dominant product. Previous studies on Ni catalysts for CO₂ hydrogenation have shown that smaller Ni nanoparticles reduce CH₄ selectivity. Similarly, our previous work on NiP_x demonstrated that phosphorization of Ni suppressed strong CO adsorption at the hollow sites of metallic Ni surfaces, thereby promoting high selectivity for CO [48]. In the present study, the weak CO adsorption is likely due to the lack of long-range lattice ordering in Co clusters, which eliminates multi-bound CO adsorption, as indicated by the DRIFTS results. In contrast, the Co NPs/TiO₂ catalyst, with its stronger CO adsorption, enables further hydrogenation of CO to CH₄. Additionally, while CoO_x clusters are more easily reduced than atomically dispersed Co, they are still less reducible than surface Co in nanoparticles, which may limit their ability to activate H₂ for CO₂ methanation [49].

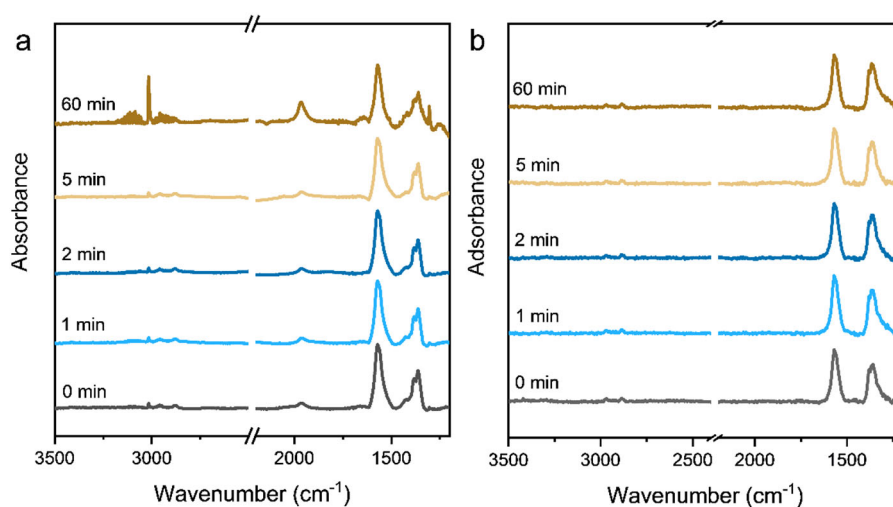


Figure 5. DRIFTS spectra of (a) Co NPs/TiO₂ and (b) Co-TiO₂-500 (12%) in CO₂ hydrogenation reaction gas with a flow rate of 10 mL min⁻¹ at 300 °C for 0–60 min.

3. Conclusions

In summary, we have developed a phase segregation strategy to achieve high CO selectivity in CO₂ hydrogenation through the formation of Co clusters on TiO₂. A thorough structural analysis, including SXR, XANES, and H₂-TPR, confirms that Co phase segregation from Co-TiO₂ occurs during high-temperature calcination, leading to the formation of small Co clusters. Compared to Co nanoparticles, our structural and catalytic performance data have demonstrated that Co clusters exhibit significantly higher selectivity for CO production. This improved activity and selectivity are attributed to their weaker interaction with the key reaction intermediate *CO, which reduces multi-bound CO adsorption, thereby suppressing methanation and greatly enhancing CO selectivity. We anticipate that this catalyst design strategy can be applied to develop highly efficient supported catalysts for selective CO₂ hydrogenation and other reactions.

Supplementary Materials: The additional data and information can be downloaded at: <https://www.sciltp.com/journals/mi/2025/1/585/s1>. Experimental section. Figure S1: TEM images of Co-TiO₂ and TiO₂ nanorods with different doping level. Figure S2: TEM images of as-synthesized Co NPs and Co NPs/TiO₂. Figure S3: TEM images of Co-TiO₂ after calcination at different temperature. Figure S4: XRD patterns of Co-TiO₂ after calcination at 500 °C and after catalytic reaction at 450 °C and the Bragg positions for anatase, brookite, and rutile TiO₂ respectively. Figure S5: XRD pattern of Co-TiO₂ after calcination at 600 °C and the Bragg positions for anatase and rutile TiO₂, respectively. Figure S6: TEM image of Co-TiO₂-500 after the stability test. Figure S7: Catalytic data of Co-TiO₂-500 with different doping level. Figure S8: Catalytic data of Co-TiO₂ treated with different calcination conditions. Figure S9: XRD patterns of Co NPs/TiO₂ after catalytic reaction at 400 °C and the Bragg positions for cobalt, anatase TiO₂, and rutile TiO₂. References [32–34,50] are cited in the supplementary materials.

Author Contributions: X.W.: conceptualization, methodology, investigation, data curation, validation, writing—original draft, writing—reviewing and editing; Y.C.: investigation, data curation, writing—reviewing and editing; Y.Z.: data curation, writing—reviewing and editing; L.Z.: data curation, writing—reviewing and editing; L.M.: methodology, data curation, writing—reviewing and editing; M.M.Y.: conceptualization, methodology, writing—reviewing and editing; S.Z.: conceptualization, methodology, resources, supervision, writing, reviewing, and editing. All authors have read and agreed to the published version of the manuscript.

Funding: The analysis of catalytic properties in this study was supported by the U.S. Department of Energy, Office of Energy Efficiency and Renewable Energy, Bioenergy Technologies Office under grant #DE-EE0009772. Support for the catalyst synthesis and structural characterization was provided by the U.S. Department of Energy, Office of Basic Energy Sciences, Chemical Sciences, Geosciences, and Biosciences Division under grant #DE-SC00234430. This research used resources 7-BM of the National Synchrotron Light Source II, a U.S. Department of Energy Office of Science User Facility operated for the DOE Office of Science by Brookhaven National Laboratory under Contract No. DE-SC0012704.

Data Availability Statement: The data that support the findings of this study are available from the corresponding author, S.Z., upon reasonable request.

Conflicts of Interest: The authors declare no conflict of interest.

References

1. Ra, E.C.; Kim, K.Y.; Kim, E.H.; Lee, H.; An, K.; Lee, J.S. Recycling carbon dioxide through catalytic hydrogenation: recent key developments and perspectives. *ACS Catal.* **2020**, *10*, 11318–11345. <https://doi.org/10.1021/acscatal.0c02930>.
2. Tackett, B.M.; Gomez, E.; Chen, J.G., Net reduction of CO₂ via its thermocatalytic and electrocatalytic transformation reactions in standard and hybrid processes. *Nature Catal.* **2019**, *2*, 381–386. <https://doi.org/10.1038/s41929-019-0266-y>.
3. Roy, S.; Cherevotan, A.; Peter, S.C. Thermochemical CO₂ hydrogenation to single carbon products: scientific and technological challenges. *ACS Energy Lett.* **2018**, *3*, 1938–1966. <https://doi.org/10.1021/acsenerylett.8b00740>.
4. Ye, R.P.; Ding, J.; Gong, W.; Argyle, M.D.; Zhong, Q.; Wang, Y.; Russell, C.K.; Xu, Z.; Russell, A.G.; Li, Q.; et al. CO₂ hydrogenation to high-value products via heterogeneous catalysis. *Nat. Commun.* **2019**, *10*, 5698. <https://doi.org/10.1038/s41467-019-13638-9>.
5. Orege, J.I.; Wei, J.; Ge, Q.; Sun, J. Spinel-structured nanocatalysts: New opportunities for CO₂ hydrogenation to value-added chemicals. *Nano Today* **2023**, *51*, 101914. <https://doi.org/10.1016/j.nantod.2023.101914>.
6. Len, T.; Luque, R. Addressing the CO₂ challenge through thermocatalytic hydrogenation to carbon monoxide, methanol and methane. *Green Chem.* **2023**, *25*, 490–521. <https://doi.org/10.1039/d2gc02900f>.
7. Cheng, K.; Li, Y.; Kang, J.; Zhang, Q.; Wang, Y. Selectivity control by relay catalysis in CO and CO₂ hydrogenation to multicarbon compounds. *Acc. Chem. Res.* **2024**, *57*, 714–725. <https://doi.org/10.1021/acs.accounts.3c00734>.
8. Yang, H.; Zhang, C.; Gao, P.; Wang, H.; Li, X.; Zhong, L.; Wei, W.; Sun, Y. A review of the catalytic hydrogenation of carbon dioxide into value-added hydrocarbons. *Catal. Sci. Technol.* **2017**, *7*, 4580–4598. <https://doi.org/10.1039/C7CY01403A>.
9. Liao, W.; Yue, M.; Chen, J.; Wang, Z.; Ding, J.; Xu, Y.; Bai, Y.; Liu, X.; Jia, A.; Huang, W.; et al. Decoupling the interfacial catalysis of CeO₂-supported rh catalysts tuned by CeO₂ morphology and Rh particle size in CO₂ hydrogenation. *ACS Catal.* **2023**, *13*, 5767–5779. <https://doi.org/10.1021/acscatal.3c00512>.
10. Karelavic, A.; Ruiz, P. CO₂ hydrogenation at low temperature over Rh/γ-Al₂O₃ catalysts: Effect of the metal particle size

- on catalytic performances and reaction mechanism. *Appl. Catal. B Environ.* **2012**, *113–114*, 237–249. <https://doi.org/10.1016/j.apcatb.2011.11.043>.
11. An, Z.; Ma, N.; Xu, Y.; Yang, H.; Zhao, H.; Wu, L.; Tan, L.; Zou, C.; Meng, F.; Zhang, B.; et al. Shape dependency of CO₂ hydrogenation on ceria supported singly dispersed Ru catalysts. *J. Catal.* **2024**, *429*, 115245. <https://doi.org/10.1016/j.jcat.2023.115245>.
 12. Chen, M.; Liu, L.; Chen, X.; Qin, X.; Li, K.; Zhang, J.; Bao, X.; Ma, L.; Zhang, C. Effects of Ru particle size over TiO₂ on the catalytic performance of CO₂ hydrogenation. *Appl. Surf. Sci.* **2024**, *654*, 159460. <https://doi.org/10.1016/j.apsusc.2024.159460>.
 13. Li, S.; Xu, Y.; Wang, H.; Teng, B.; Liu, Q.; Li, Q.; Xu, L.; Liu, X.; Lu, J. Tuning the CO₂ hydrogenation selectivity of rhodium single-atom catalysts on zirconium dioxide with alkali ions. *Angew. Chem. Int. Ed.* **2023**, *62*, e202218167. <https://doi.org/10.1002/anie.202218167>.
 14. Galhardo, T.S.; Braga, A.H.; Arpini, B.H.; Szanyi, J.; Goncalves, R.V.; Zornio, B.F.; Miranda, C.R.; Rossi, L.M. Optimizing active sites for high CO selectivity during CO₂ hydrogenation over supported nickel catalysts. *J. Am. Chem. Soc.* **2021**, *143*, 4268–4280. <https://doi.org/10.1021/jacs.0c12689>.
 15. Vogt, C.; Groeneveld, E.; Kamsma, G.; Nachtegaal, M.; Lu, L.; Kiely, C.J.; Berben, P.H.; Meirer, F.; Weckhuysen, B.M. Unravelling structure sensitivity in CO₂ hydrogenation over nickel. *Nat. Catal.* **2018**, *1*, 127–134. <https://doi.org/10.1038/s41929-017-0016-y>.
 16. Cao, F.; Song, Z.; Zhang, Z.; Xiao, Y.S.; Zhang, M.; Hu, X.; Liu, Z.W.; Qu, Y. Size-controlled synthesis of Pd nanocatalysts on defect-engineered CeO₂ for CO₂ hydrogenation. *ACS Appl. Mater. Interfaces* **2021**, *13*, 24957–24965. <https://doi.org/10.1021/acsami.1c05722>.
 17. Simons, J.F.M.; de Heer, T.J.; van de Poll, R.C.J.; Muravev, V.; Kosinov, N.; Hensen, E.J.M. Structure sensitivity of CO₂ hydrogenation on Ni revisited. *J. Am. Chem. Soc.* **2023**, *145*, 20289–20301. <https://doi.org/10.1021/jacs.3c04284>.
 18. Zhang, R.; Wang, X.; Wang, K.; Wang, H.; Song, S.; Zhang, H. Effects of metal size on supported catalysts for CO₂ hydrogenation. *Mater. Chem. Front.* **2023**, *7*, 6411–6426. <https://doi.org/10.1039/d3qm00384a>.
 19. Adhikari, D.; Whitcomb, C.A.; Zhang, W.; Zhang, S.; Davis, R.J. Revisiting the influence of Ni particle size on the hydrogenation of CO₂ to CH₄ over Ni/CeO₂. *J. Catal.* **2024**, *438*, 115708. <https://doi.org/10.1016/j.jcat.2024.115708>.
 20. Niu, K.; Chen, L.; Rosen, J.; Björk, J. CO₂ hydrogenation with high selectivity by single Bi atoms on MXenes enabled by a concerted mechanism. *ACS Catal.* **2024**, *14*, 1824–1833. <https://doi.org/10.1021/acscatal.3c04480>.
 21. Swallow, J.E.N.; Jones, E.S.; Head, A.R.; Gibson, J.S.; David, R.B.; Fraser, M.W.; van Spronsen, M.A.; Xu, S.; Held, G.; Eren, B.; et al. Revealing the role of CO during CO₂ hydrogenation on Cu surfaces with In Situ soft X-Ray spectroscopy. *J. Am. Chem. Soc.* **2023**, *145*, 6730–6740. <https://doi.org/10.1021/jacs.2c12728>.
 22. Kattel, S.; Liu, P.; Chen, J.G. Tuning selectivity of CO₂ hydrogenation reactions at the metal/oxide interface. *J. Am. Chem. Soc.* **2017**, *139*, 9739–9754. <https://doi.org/10.1021/jacs.7b05362>.
 23. Zhang, J.; Yang, Y.; Liu, J.; Xiong, B. Mechanistic understanding of CO₂ hydrogenation to methane over Ni/CeO₂ catalyst. *Appl. Surf. Sci.* **2021**, *558*, 149866. <https://doi.org/10.1016/j.apsusc.2021.149866>.
 24. Yang Lim, J.; McGregor, J.; Sederman, A.J.; Dennis, J.S. Kinetic studies of CO₂ methanation over a Ni/γ-Al₂O₃ catalyst using a batch reactor. *Chem. Eng. Sci.* **2016**, *141*, 28–45. <https://doi.org/10.1016/j.ces.2015.10.026>.
 25. Song, J.; Chen, B.; Bian, J.; Cai, Y.; Ali, S.; Cai, D.; Zheng, B.; Huang, J.; Zhan, G. ZnZrO_x nanoparticles derived from metal–organic frameworks as superior catalysts to boost CO₂ hydrogenation to methanol. *ACS Appl. Nano Mater.* **2024**, *7*, 19677–19687. <https://doi.org/10.1021/acsanm.4c03801>.
 26. Li, K.; Li, X.; Li, L.; Chang, X.; Wu, S.; Yang, C.; Song, X.; Zhao, Z.-J.; Gong, J. Nature of catalytic behavior of cobalt oxides for CO₂ hydrogenation. *JACS Au* **2023**, *3*, 508–515. <https://doi.org/10.1021/jacsau.2c00632>.
 27. Struijs, J.J.C.; Muravev, V.; Verheijen, M.A.; Hensen, E.J.M.; Kosinov, N. Ceria-supported cobalt catalyst for low-temperature methanation at low partial pressures of CO₂. *Angew. Chem. Int. Ed. Engl.* **2023**, *62*, e202214864. <https://doi.org/10.1002/anie.202214864>.
 28. Wang, L.; Guan, E.; Wang, Y.; Wang, L.; Gong, Z.; Cui, Y.; Meng, X.; Gates, B.C.; Xiao, F.-S. Silica accelerates the selective hydrogenation of CO₂ to methanol on cobalt catalysts. *Nat. Commun.* **2020**, *11*, 1033. <https://doi.org/10.1038/s41467-020-14817-9>.
 29. Rahmati, M.; Safdari, M.S.; Fletcher, T.H.; Argyle, M.D.; Bartholomew, C.H. Chemical and thermal sintering of supported metals with emphasis on cobalt catalysts during Fischer-Tropsch synthesis. *Chem. Rev.* **2020**, *120*, 4455–4533. <https://doi.org/10.1021/acs.chemrev.9b00417>.
 30. Liu, S.; He, Y.; Fu, W.; Chen, J.; Ren, J.; Liao, L.; Sun, R.; Tang, Z.; Mebrahtu, C.; Zeng, F. Hetero-site cobalt catalysts for higher alcohols synthesis by CO₂ hydrogenation: A review. *J. CO₂ Util.* **2023**, *67*, 102322. <https://doi.org/10.1016/j.jcou.2022.102322>.
 31. Miyazaki, R.; Belthle, K.S.; Tüysüz, H.; Foppa, L.; Scheffler, M. Materials genes of CO₂ hydrogenation on supported cobalt catalysts: An artificial intelligence approach integrating theoretical and experimental data. *J. Am. Chem. Soc.* **2024**,

- 146, 5433–5444. <https://doi.org/10.1021/jacs.3c12984>.
32. Zhang, Z.; Wu, Q.; Johnson, G.; Ye, Y.; Li, X.; Li, N.; Cui, M.; Lee, J.D.; Liu, C.; Zhao, S.; et al. Generalized synthetic strategy for transition-metal-doped brookite-phase TiO₂ nanorods. *J. Am. Chem. Soc.* **2019**, *141*, 16548–16552. <https://doi.org/10.1021/jacs.9b06389>.
 33. Liu, C.; Qian, J.; Ye, Y.; Zhou, H.; Sun, C.-J.; Sheehan, C.; Zhang, Z.; Wan, G.; Liu, Y.-S.; Guo, J.; et al. Oxygen evolution reaction over catalytic single-site Co in a well-defined brookite TiO₂ nanorod surface. *Nat. Catal.* **2021**, *4*, 36–45. <https://doi.org/10.1038/s41929-020-00550-5>.
 34. Wu, L.; Li, Q.; Wu, C.H.; Zhu, H.; Mendoza-Garcia, A.; Shen, B.; Guo, J.; Sun, S. Stable Cobalt nanoparticles and their monolayer array as an efficient electrocatalyst for oxygen evolution reaction. *J. Am. Chem. Soc.* **2015**, *137*, 7071–7074. <https://doi.org/10.1021/jacs.5b04142>.
 35. Liu, Q.; Jiang, Y.; Yan, W.; Sun, Z.; Pan, Z.; Yao, T.; Wu, Z.; Wei, S. Co-doped rutile TiO₂- δ thin films studied by XANES and first principles calculations. *J. Phys. Conf. Ser.* **2009**, *190*, 012107. <https://doi.org/10.1088/1742-6596/190/1/012107>.
 36. Bao, S.; Yang, L.; Fu, H.; Qu, X.; Zheng, S. Fine Ru-Ru₂P heterostructure enables highly active and selective CO₂ hydrogenation to CO. *ACS Catal.* **2024**, *14*, 18134–18144. <https://pubs.acs.org/doi/full/10.1021/acscatal.4c05369>.
 37. Zhou, X.; Price, G.A.; Sunley, G.J.; Copéret, C. Small cobalt nanoparticles favor reverse water-gas shift reaction over methanation under CO₂ hydrogenation conditions. *Angew. Chem. Int. Ed. Engl.* **2023**, *62*, e202314274. <https://doi.org/10.1002/ange.202314274>.
 38. Yan, Y.; Liu, C.; Jian, H.; Cheng, X.; Hu, T.; Wang, D.; Shang, L.; Chen, G.; Schaaf, P.; Wang, X.; et al. Substitutionally dispersed high-oxidation CoO_x clusters in the lattice of rutile TiO₂ triggering efficient Co-Ti cooperative catalytic centers for oxygen evolution reactions. *Adv. Funct. Mater.* **2020**, *31*, 2009610. <https://doi.org/10.1002/adfm.202009610>.
 39. Zhou, T.; Xu, W.; Zhang, N.; Du, Z.; Zhong, C.; Yan, W.; Ju, H.; Chu, W.; Jiang, H.; Wu, C.; et al. Ultrathin cobalt oxide layers as electrocatalysts for high-performance flexible Zn-Air batteries. *Adv. Mater.* **2019**, *31*, e1807468. <https://doi.org/10.1002/adma.201807468>.
 40. Mori, K.; Jida, H.; Kuwahara, Y.; Yamashita, H. CoO_x-decorated CeO₂ heterostructures: Effects of morphology on their catalytic properties in diesel soot combustion. *Nanoscale* **2020**, *12*, 1779–1789. <https://doi.org/10.1039/c9nr08899g>.
 41. Wang, X.; Du, L.Y.; Du, M.; Ma, C.; Zeng, J.; Jia, C.J.; Si, R. Catalytically active ceria-supported cobalt-manganese oxide nanocatalysts for oxidation of carbon monoxide. *Phys. Chem. Chem. Phys.* **2017**, *19*, 14533–14542. <https://doi.org/10.1039/c7cp02004j>.
 42. Savereide, L.; Gosavi, A.; Hicks, K.E.; Notestein, J.M. Identifying properties of low-loaded CoO_x/CeO₂ via X-ray absorption spectroscopy for NO reduction by CO. *J. Catal.* **2020**, *381*, 355–362. <https://doi.org/10.1016/j.jcat.2019.11.016>.
 43. Li, J.; Lu, G.; Wu, G.; Mao, D.; Guo, Y.; Wang, Y.; Guo, Y. Effect of TiO₂ crystal structure on the catalytic performance of Co₃O₄/TiO₂ catalyst for low-temperature CO oxidation. *Catal. Sci. Technol.* **2014**, *4*, 1268–1275. <https://doi.org/10.1039/c3cy01004j>.
 44. Platero, F.; Todorova, S.; Aoudjera, L.; Michelin, L.; Lebeau, B.; Blin, J.L.; Holgado, J.P.; Caballero, A.; Colon, G. Cobalt stabilization through mesopore confinement on TiO₂ support for Fischer-Tropsch reaction. *ACS Appl. Energy Mater.* **2023**, *6*, 9475–9486. <https://doi.org/10.1021/acsaem.3c01432>.
 45. Lima, T.M.; Castelblanco, W.N.; Rodrigues, A.D.; Roncolato, R.E.; Martins, L.; Urquieta-González, E.A. CO oxidation over Co-catalysts supported on silica-titania—The effects of the catalyst preparation method and the amount of incorporated Ti on the formation of more active Co³⁺ species. *Appl. Catal. A Gen.* **2018**, *565*, 152–162. <https://doi.org/10.1016/j.apcata.2018.08.006>.
 46. Li, W.H.; Zhang, G.H.; Jiang, X.; Liu, Y.; Zhu, J.; Ding, F.S.; Liu, Z.M.; Guo, X.W.; Song, C.S. CO₂ hydrogenation on unpromoted and M-promoted Co/TiO₂ catalysts (M = Zr, K, Cs): Effects of crystal phase of supports and metal-support interaction on tuning product distribution. *ACS Catal.* **2019**, *9*, 2739–2751. <https://doi.org/10.1021/acscatal.8b04720>.
 47. Deng, K.X.; Lin, L.L.; Rui, N.; Vovchok, D.; Zhang, F.; Zhang, S.H.; Senanayake, S.D.; Kim, T.; Rodriguez, J.A. Studies of CO₂ hydrogenation over cobalt/ceria catalysts with in situ characterization: The effect of cobalt loading and metal-support interactions on the catalytic activity. *Catal. Sci. Technol.* **2020**, *10*, 6468–6482. <https://doi.org/10.1039/d0cy00962h>.
 48. Wei, X.; Johnson, G.; Ye, Y.; Cui, M.; Yu, S.-W.; Ran, Y.; Cai, J.; Liu, Z.; Chen, X.; Gao, W.; et al. Surfactants used in colloidal synthesis modulate Ni nanoparticle surface evolution for selective CO₂ hydrogenation. *J. Am. Chem. Soc.* **2023**, *145*, 14298–14306. <https://doi.org/10.1021/jacs.3c02739>.
 49. Li, X.Y.; Lin, J.; Li, L.; Huang, Y.K.; Pan, X.L.; Collins, S.E.; Ren, Y.J.; Su, Y.; Kang, L.L.; Liu, X.Y.; et al. Controlling CO₂ hydrogenation selectivity by metal-supported electron transfer. *Angew. Chem.-Int. Ed.* **2020**, *8*, 19983–19989. <https://doi.org/10.1002/anie.202003847>.
 50. Ravel, B.; Newville, M. ATHENA, ARTEMIS, HEPHAESTUS: data analysis for X-ray absorption spectroscopy using IFEFFIT. *J. Synchrotron Radiat.* **2005**, *12*, 537–541